Design and performance of very long-wavelength $GaAs/Al_xGa_{1-x}As$ quantum-well infrared photodetectors

G. *Sarusi*, S. *D. Gunapala*[+], *J.* S. *Park*[+], *and* R *F. Levine*

AT&T Bell Laboratories, Murray Hill, NJ 07974
Murray Hill, NJ 07974

[+] Center for Space Microelectronics Technology, Jet Propulsion Laboratory, California Institute of Technology, Pasadena, CA 91109, USA

ABSTRACT

Wc present an extensive and detailed study of very long wavelength quantum wc]] infrared photodetectors covering the spectral region between 14 μm and 20 μm. Measurements were made on seven di fferent molecular beam epitaxy (MBE) grown samples having different wc]] widths and barrier heights. In this study we combine experimental results with theoretical analysis and focus on the relationship between the quantum well structu re and detector performance, i.e., responsivity, dark current, dynamic resistance, noise current, optical-gain, and detectivity. These results provide the basis for further optimization, and the detector parameters needed for the design of the readout circuit for focal plane array.

Design and performance of very long-wavelength $GaAs/Al_xGa_{1-x}As$ quantum-well infrared photodetectors

1.1 NTRODIJCTION

Very long wavelength infrared (VWIR) photodetectors, '*) covering the spectral range from 14μm to 20μm , are of great interest for a variety of space applications such as monitoring the global atmospheric temperature profile (in this spectral range the atmosphere is opaque and thus its emission can be monitored), relative humidity profile, cloud characteristics, and the distribution of minor constituents in the atmosphere. Also, this spectral region is rich in astronomical information vital to the understanding of the composition, structure and the energy balance of molecular clouds and star forming regions of our galaxy. Thus, large VWI R linear arrays and two dimensional staring arrays (128x1 28 and 256x256 pixels) are necessary for NASA's space-born platforms[2] for spectroscopic and imaging applications. These kinds of VWIR photodetectors are desirable as one dimensional arrays for spectroscopic measurements as well as two dimensional . The requirements on such detectors are demanding and become more difficult to meet as the operating wavelength becomes longer and longer. These include high defectivity ($D_\lambda^* > 10^{"}$ cm $Hz^{1/2}/W$ at 55K for a detector with a cutoff wavelength of $\lambda_c = 16\mu m$), low dark currents, low noise currents, high uniformity among detectors in the array, as well as high output impedance (above $1M\Omega$). The latter requirement is necessary for achieving high carrier injection into the readout circuit, since such arrays are usually coupled to a CMOS based readout circuit having several megohm input impedance.[3] Present state of the art $Hg_{1-x}Cd_xTe$ based detectors cannot meet these requirements. In order to have a high impedance and low dark current the

$Hg_{1-x}Cd_xTe$ detectors need to be operated in a photovoltaic mode near zero bias. However, the longest photovoltaic cutoff wavelength achieved is only 14.5pm(4), since for longer wavelengths the p-n junction characteristics are severely degraded, Thus, $Hg_{1-x}Cd_xTe$ detectors can only be operated at wavelengths longer than λ= 14.5pm in a photoconductive mode. Unfortunately $Hg_{1-x}Cd_xTe$ photoconductive detectors have a substantially lower performance due to their very low impedance, (in the range of only a few kilo-ohms) as well as the associated high dark currents that can saturate the readout circuit. In addition ,the use of surface passivation such as native sulfides and ZnS makes the $Hg_{1-x}Cd_xTe$ detectors more vulnerable to ionizing radiation.[5]

Quantum-well infrared photodetectors (QWIPs) of $GaAs/Al_xGa_{1-x}As$ are thus an attractive alternative which can overcome most of the difficulties mentioned above for this spectral region. This is due to their mature growth and processing technology and the possibility of producing uniform, high performance, large area two-dimensional imaging arrays. At λ~10μm arrays of 128x1 28 pixels as well as 256x256 and 640x480 have been demonstrated, The QWIPs have the advantage of low 1/f noise,[G] that can eliminate the need to use an optical chopper, low power dissipation, high dynamic resistance, low dark current and high radiation hardness. By carefully designing the quantum well structure as well as the light coupling to the detector it is possible to optimize the material to have an optical response in the desired spectral range, determine the spectral response shape, as well as reduce the leakage dark current and therefore increase the detector impedance. Generally, in order to *tailor* the quantum well detector's response to the very long wavelength spectral region (> 14pm) the barrier height should be lowered and the well width increased relative to shorter λ_c QWIPs.

To meet the high specifications required, the VWIR QWIPS have to be optimized for three

different aspects: material and quantum well structure; efficient light coupling; and depression of the dark current (using three terminals QWIP) and therefore the noise current.[7] Previous papers have shown several methods which have bee developed to achieve efficient light coupling using a random scattering reflector.[8] In this paper we describe the optimization of the material and quantum well (QW) structure to have the highest performance in the required spectral region. Systematic measurements were made on seven samples, grown sequentially on a well-calibrated molecular beam epitaxy (MBE) machine. 'I'he samples that differ only in their quantum well structure, (i. e., Al concentration in the barrier and well width), cover most of the important VWIR spectral regions. Temperature dependent dark current and dynamic resistance measurements as well as noise, photocurrent and spectra] responsivity measurements are combined in order to analyze in detail the relationship between the QW structure and device performance.

1 ISAMPLE DESIGN, GROWTH AND PROCESSING

For QWIPs operating in the 8-12pm spectral range the well widths are approximately 40Å and the Al concentration in the barriers is about x-30°/0.(9) Generally, in order to *tailor* the quantum well detector's spectral-response to the very long wavelength spectral region, the barrier height should be lowered and the well width to be increased thereby reducing the transition energy between the first and the second energy states in the well.[10,11] Reducing the Al concentration in the barrier to reduce the energy separation between the levels is not sufficient, since in this case the second level will be pushed high into the continuum by that increasing the dark current, lowering the detector impedance and substantially broadening the spectrum. To

lower the continuum state to be just under the top of the barrier, the well width should be increased simultaneously with reducing the barrier height. This will maximize the bound-to-bound intersubband absorption, while maintaining the excellent hot electron transport properties. In Addition, in order to further reduce the dark current and increase the dynamic resistance the Fermi level should be lowered to be only few meV (4 to 6meV) above the first energy state in the well, For a given QW width, this can be achieved by lowering the doping level in the well to be just above the freeze-out level at the operating temperature.

With these considerations in mind, seven samples were grown by QED Inc. on 3 inche semi-insulating GaAs substrates using the MBE growth technique. Each sample consisted of 50 periods of quantum wells, Si-doped $N_D = 2.5 \times 10^{17} cm^{-3}$, with barrier thicknesses of $L_b = 600Å$ and well width of 72Å and 66Å sandwiched between 2.3pm top and 0.8μm bottom contact layers doped to $N_D = 2.5 \times 10^{17} cm^{-3}$, (The top layer was grown thick to allow for gratings). The various samples differed only in their well widths and Al concentrations in the barriers (i. e., barrier height), which are presented in Table 1. In order to keep the accuracy of 0.5% in the Al concentration all the samples were grown sequentially with the same calibration. Photoconductive detectors having $200 \times 200 \mu m^2$ mesa area were fabricated using standard photolithography. In order to determine the influence of the different QW structure on the detector characteristics, light coupling was made by illuminating the detectors through a 45° face polished on the substrate, thus avoiding any possible variation in grating coupling.

1 I 1. RESPONSIVITY MEASUREMENTS

The responsivity wavelength spectra R(A) of the seven samples were measured using a

polished 45° incident facet together with a globar source and a monochrometer. A dual lock-in ratio system (using a spectrally flat pyroclectric detector) was used to normalize the system spectral response. The absolute value of the responsivity was determined by measuring the photocurrent 1_p with a calibrated blackbody source. Responsivity measurements were taken at T= 10K for convenience, but no significant change of the responsivity curves was detected up to T=60K. Figure 1 shows the normalized responsivity spectra R(λ)for the seven different samples measured at -3V and over the 12-20μm wavelength range. This figure clearly demonstrates the high controllability and accuracy of the MBE grown QWIPs even for the very long wavelengths, covering the spectral range between 14-20pm. Samples 1 -4 and 5-7 differ by only 0.5% in the Al concentration of the barrier, while the difference between samples 4 and 5 (having the same Al concentration x=-1 4.5°/0) is in the well widths of $I._w$ = 72Å and 66Å, respectively. All spectra were measured over the wider wavelength range of 6-20μm and the full spectra of three different samples is shown in Fig.2, demonstrating the relatively narrow spectral bandwidth of A λ/λ= 15°/0. 'l"able II contains the measured values of peak λ_p and cutoff λ_c wavelength, full width half maximum (AA), as well as the absolute responsivity values (in both A/W and V/W).

The responsivity value for sample ***7*** of ***87300*** V/W is the *highest* responsivity reported in this wavelength range. Higher current responsivity values (in A/W) can be achieved by increasing the bias, but the tradeoff is a decrease in the dynamic resistance. For those applications where a high photocurrent is needed the QWIPs can be operated at a higher bias. Fig 3 shows the peak current responsivity R_p in A/W as a function of bias for the different samples.

It can be seen that generally at low bias (V_b<|2|V) the dependence of R_p on bias is sublinear indicating that the second energy state is weakly bound, i.e., the excited state is nearly resonant

with the top of the barrier. For each sample the position of the first and the second energy state as well as the barrier edge was calculated; "l'able 111 presents the calculated results for the energy level of the first and the second bound state and the barrier height for each sample. As expected, it can be seen that the second energy state is only slightly under the top of the barrier edge, Comparing the responsivity of samples 4 and 5 (both having 14.5% Al in the barrier but with L_W=72Å and 66Å, respectively), shows that the latter has nearly two times higher current responsivity in A/W. This can be easily understood since for the 66Å well sample the second energy level is more weakly bound, thereby increasing the electrons escape probability from the wells and hence the photocurrent. Consistent with this explanation, the dynamic resistance is lower, and thus the voltage responsivity values in V/W (as seen in Table 11) are similar.

Figure 4 shows the peak wavelength plotted against the barrier Al concentration, The agreement between the experimental and the calculated results is very good, typically being within 4meV. This small difference can be easily attributed to a 1Å variation in the well width or a 0.2% difference in the barrier Al concentration.

IV. DARK CURRENT, BACKGROUND P11OTOC1JRRENT ANI) DYNAMIC RESISTANCE

The dark current i_D and dynamic resistance play a crucial roll in determining the ultimate performance of the individual detectors in the array. Therefore, we did detailed measurements of the temperature dependence of the dark current vs. voltage on 200x200μm^2 mesa devices. These measurements were made using a cold shield that completely surrounded and was stabilized to be the same temperature as that of the QWIP. The background photocurrent was measured while

the sample was maintained at 10K but exposed to the room temperature T= 300K background flux through a KRS-5 window (also at room temperature) and 180° field of view. Figures 5, 6, 7 and 8 show the temperature dependence of the dark current-voltage curves for samples 1, 4, 5, and 7 and the 300K background photocurrent is shown by the dashed curve. For all samples thermionic emission is the dominant current mechanism down to T= 25-30K, which is evident by the exponential decrease of the dark current with temperature. The magnitude of this dark current strongly depends on the QW structure, i.e., barrier height and well width. By comparing these window photocurrents (at -2V) and the temperature dependent dark current $i_D(T)$, the temperature T_{BLIP} at which these detectors are background limited (BLIP) can be determined and are shown in Table IV.

Close inspection shows that the background photocurrent does not change much from sample to sample. The main contribution to the increase in the BLIP temperature is the decrease in the dark current at shorter wavelengths. From the curves in figs. 5 to 8 it can be seen that for very low bias (V_b<|1|V) the BLIP temperature is higher. This fact however does not necessarily mean that the highest defectivity will be obtained at this very low bias since the responsivity drops sharply due to the high capture probability of the excited electrons back to the well. As will be shown in the next section the maximum defectivity in these samples was obtained between -2V and -3V.

In order to more clearly observe the exponential dark current behavior with bias and temperature, the data were replotted as a function of 1/T for different biases. One example is shown in Fig. 9 for sample 7. It is evident that for low biases up to -3V, thermal activation determines the dark current due to the thermionic emission of electrons out of the well. This

region is represented by the straight line in the plot of $\log(I_D)$ vs. 1/'1' down to T= 33K. The flat part of the curve is due to the onset of tunneling, which occurs at T<25K but can also be distinguished at higher temperature for higher bias. Most of this current is associated with thermally assisted tunneling through the barrier tip. At very low temperatures (T<25K) the current tends to saturate for all the samples (as seen also in Figs. 5-8) at around 8×10^{-12}Amp. This current saturation is attributed to trap assisted tunneling, in which the electrons tunnel through impurity states located in the barriers. It should be mentioned that this trap assisted tunneling can be eliminated by a more careful control of the barrier quality during the growth, although it does not affect the device performance when operating above 30K. This kind of tunneling is most common in intrinsic narrow band-gap semiconductors such as $Hg_{1-x}Cd_xTe$ at temperatures lower than 70K, which prevents significant improvement in their performance by further cooling, even with λ_c -10μm.[12] In our case substantial improvement can be achieved by cooling the device down to 30K, as will be presented in the next section.

At low bias (where tunneling is negligible) the dark current I_D is expected to increase exponentially with temperature following:

$$I_D \alpha Te^{-\Delta E/kT} \qquad (1)$$

with the thermal activation energy given by $\Delta E = E_C - E_F$, where k is Boltzmann constant and T is the absolute temperature in Kelvin. In order to examine this dependence in detail, the current-voltage curves of all seven samples were replotted in Fig. 10 for V_b=-2V as $\log(I_D / T)$ vs. 1000/T which is the temperature normalized current. As expected, the normalized dark current $\log(I_D / T)$ plotted against inverse temperature follows an excellent straight line for all the samples and from

the slope of this line we determine ΔE. Based on the responsivity measurements discussed above, the cutoff wavelength λ_c was determined for each sample and the corresponding cutoff energy E_C determined from $E_c = hc/\lambda_c$ where h is Planks constant and c is the speed of light . The Fermi level E_F of the two dimensional electron gas in the well can be obtained from:

$$N_D = n_0 \ln(1 + e^{E/kT}) \tag{2}$$

and

$$n_0 = m^* kT/\pi h^2 L_W \tag{3}$$

where N_D is the doping density in the well, m* is the electron effective mass and L_W is the well width. Combining E_C with the Fermi energy obtained from these calculations, E_F = 6.5meV for the 72Å ***wells*** and 5.9meV for the 66Å wells for $N_D = 2.5 \times 1017\ cm^{-3}$, ΔE can be determined and is compared in 'I'able V to the values obtained from the slope of the dark current curves of Fig. 10. As can be seen from the table there is a very good agreement between the values obtained from the spectra (λ_c) and that obtained from the dark current measurements assuming thermal activation in this temperature range. Note that ΔE increases with increasing Al concentration in the barriers as can be seen for samples 1-4 and for samples 5-7. Figure 11 presents this comparison in terms of cutoff wavelength.

The dynamic resistance which is governed by the same mechanisms as the dark current plays a crucial roll for coupling the focal plane array to the readout circuits. For typical CMOS readout circuits a detector output impedance of more than MΩ is needed in order to work in the

direct injection mode without buffer circuits and electronic choppers, Figure 12 shows the dynamic resistance at -2V for 200x200μm^2 mesa devices for the different samples as a function of inverse temperature (1/T). As with the dark current a straight line is evident for temperatures above 33K for all the samples, The effect of tunneling can be seen at very low temperatures (T<30K) by the tendency toward saturation. As is expected, the dynamic resistance drops with an increase in the cutoff wavelength, but nevertheless it can be seen that 1MΩ and higher output impedances can be achieved by cooling the samples from 50K to 40K, depending on the cutoff wavelength (λ_c =15.9-18.6pnl). In this temperature range most of the Si based multiplexers can work without any modification in a direct injection mode. It should be noted that higher dynamic resistance (and lower dark current) can be achieved for the same cutoff wavelength by designing the structure to have a bound-to-bound transition in which the second energy level is more than ~4meV below the top of the barrier. This can be accomplished by increasing the Al concentration in the barrier and at the same time increasing the well width. However, the trade off in this case will be a decrease in the responsivity but not necessary in the defectivity since the dark current and the shot noise also decrease strongly.

V. NOISE CURRENT AND OPTICAL GAIN

The noise current was measured directly using a spectrum analyzer under dark conditions, i.e. a cold shield surrounding the QWIP. It was found that similar results were also obtained by measuring the dark noise and photocurrent noise under BLIP conditions. For most of the samples the noise measurements were done at 55K as a function of bias. At this temperature the devices are not BLIP and thus the dominant noise mechanism is shot noise. The optical gain g can be

obtained using the photocurrent shot-noise expression (valid for small quantum well capture probability, i.e., $p_c << 1$)

$$i_n = \sqrt{4eI_D g \Delta f} \qquad (4)$$

where I_D is the dark current g is the gain and Af is the frequency bandwidth in which the noise was measured. In order to obtain the dark current shot noise, system noise and Johnson noise were subtracted from the total measured noise using:

$$i_n^2(shot) = i_n^2(measured) - i_n^2(system) - i_n^2(Johnson) \qquad (5)$$

Figure 13 shows the measured bias dependent dark current shot noise at 55K for all of the samples. As expected the noise increases super-linearly with the bias and is inversely proportional to the barrier height. Comparing the shot noise of sample 4 (L_W = 72Å) to Sample 5 (L_W = 66Å), having the same Al concentration in the barrier (14, 5%), it can be seen that sample 4 has nearly half of the shot noise current of sample 5,

The optical gain can be deduced from Eq. 4 (for low p_c), and Fig. 14 shows the optical gain obtained for samples 1 and 7 (that represent the spectral extremes of the seven samples) as a function of the bias. For both samples the gain increases with the bias with a plateau between 1 and 3V near g = 0.1 and then increases rapidly with the bias, For a 50 QW structure gain of a 0.1 is equivalent to a hot electron mean free path of 5 QW periods, i.e., around 3350Å, and therefore corresponds to a capture probability of p_c = 0.2, For $V_b > 3V$ the super-linear increase in the gain is

due to avalanche multiplication of the high energy electrons. It should be mentioned that higher gains should be achievable by further optimizing the growth conditions (i.e. higher growth temperature) in order to improve the AlGaAs barrier quality, and thus increase the hot electron mobility.

VI. DETECTIVITY

Combining the responsivity values determined in section 11 and the noise currents from section V, the defectivity D^*_λ can be obtained from:

$$D^*_\lambda = \frac{R_p}{i_n}\sqrt{A\,\Delta f} \qquad (6)$$

Fig. 15 shows the bias dependence of D^*_λ for sample 7 at 55K, which increases with bias up to -2V The detectivity reaches a maximum of $D^*_\lambda = 1.7 \times 10^{10}$ cm $Hz^{0.5}/W$ and then starts to decrease when the bias is increased further, due to the increase in the dark current and therefore the noise current. It should be mentioned that although the responsivity also increases with bias at high voltage, the increasing noise dominates and determines the defectivity values. For a QWIP at 55K having a cutoff wavelength of 15.9μm the value of $D^*_\lambda = 1.7 \times 10^{10}$ cm $Hz^{0.5}/W$ is the *highest* value ever achieved using a 45° polished edge configuration.

In a similar way the D^*_λ values for the other samples were obtained, and these values arc presented in Fig. 15 for T = 55K and V_b = -2V. The values of D^*_λ for the different samples are plotted in term of the peak wavelength corresponding to each sample. An exponential decrease in D^*_λ is observed as the sample wavelength increases which is expected for devices with dark

current governed by thermal mechanisms. For these QWIPs covering the VW] R spectral region (14 to 20μm) D^*_λ varies from 2 x 10'^{0} to 3 x 10' cm $Hz^{0.5}$/W at 55K. Further increases in the detectivity can be expected by a further optimization of the structures. In addition, by combining these QWIPs with an efficient light coupler such as a 2D grating with optical cavity, or a random scattering reflector these values of D^*_λ will increase by factor 4 to 8, respectively.tl^{5,x}j

VJ 1. SUMMARY AND CONCLUSION .

in this study we have presented experimental results characterizing very long wavelength quantum well infrared photodetectors in the 14pm to 20pm spectral range. As was emphasized throughout this work, QWIPs allow many degrees of freedom to *tailor* the performance to users specifications. By extrapolating the D^*_λ results of sample 7 (λ_p~15pm) measured at 55K to a lower temperature of 40K, a D^*_λ of 3 x 10^{12} cm $Hz^{0.5}$/W can be achieved. This high D^*_λ can be further increased by the use of a proper optical coupler, i.e., a ***2D*** grating or random scatterer. For focal plane arrays, detector areas of 50x50μm^2 to 30x30μm^2 can be used. For these size pixels QWIPs with λ_p~15pm can work in the direct injection mode with a conventional CMOS readout circuit since the dark current would be less than 6pA per pixel and the dynamic resistance more then 3GΩ. It should be mentioned that fabricating gratings on these detectors (2D or random scatterer) would increase in the defectivity by four to eight times. Such light couplers also provide more degrees of freedom. One can optimize the detectors for a 15pm peak response by designing the QWIP to have a transition at λ_p=14.5μm. The spectral correction toward 15pm can than be made by designing the grating, i.e., the period in 2D gratings and the step height in the random scatterer) to peak at 15.5μm. The spectral response will be a convolution of the two effect, giving

rise to a peak around 15pm. The benefit in this optimization is that the dark current and dynamic resistance will be substantially improved.

ACKNOWLEDGMENTS

The research described in this paper was jointly sponsored by the Ballistic Missile Defense Organization/Innovative Science and Technology Office, and the National Aeronautics and Space Administration, Office of Advanced Concepts and I'ethnology.

REFERENCES

(1) B.F. Levine, J. Appl. Phys. 74, R1(1993)

(2) M. T. Chahine, Proceedings of innovative long wavelength infrared detectors workshop, Pasadena, CA, April 24-26, (1990)

(3) C. G. Bethea, B. F. Levine, M. T. Asom, R. E. Leibenguth, J, W. Stayt, K. G. Glogovsky, R. A, Morgan, J. Blackwell and W. Parrish, IEEE Trans. Elect. Devices 40,1 957(1993)

(4) The 1993 U.S. workshop on the physics and chemistry of mercury cadmium telluride and other IR materials. October, 19, 1993. Seattle, Washington

(5) G. Sarusi, D. Eger, A. Zemel, N. Mainzer, R, Goshen and E. Weiss, IEEE Trans. Nucl. Scie. 37,2042 (1 990)

(6) 1.. J. Kozlowski, G. M. Williams, G. J. Sullivan, C. W. Parley, R. J. Andersson, D.T. Cheung, W. 13. Tennant and R. E. DeWames, IEEE Trans. Electon, Devices ED-38, 24(1991)

(7) K. K. Choi, M. Dutta, P.G. Newman , L. Calderon, W. Chang and G. J. Iafrate, Phys. Rev. B42, 9166(1990)

(8) G. Sarusi, B. F. Levine, S. J. Pearton, K.M.S. Bandara and R. E. Leibenguth, Appl. Phys. Lett. ***64, 960(1994)***

(9) K. K. Choi, J. Appl. Phys. 73,5230(1993)

(10) A. Zussman, B.F. Levine, J. M. Kuo and J. de Jong, J. Appl. Phys. 70,51 01(1 991)

(11) B. F. Levine, A. Zussman, J. M. Kuo and J. de Jong, J. Appl. Phys. 71,5130(1992)

(12) ***Y.*** Nemirovsky, D. Rosenfeld, R. Adar and A. Korenfeld, J. Vat, Sci. Technol. A1,1949(1983)

(13) J. Y, Andersson, L. Lundqvist and Z. F. Paska, Appl. Phys. Lett. 58,2264(1 991)

FIGURE CAPTIONS

Fig. 1: Normalized spectral response curves ($1\ 2\mu m < \lambda < 20\mu m$) of the seven different samples

Fig. 2: Normalized spectral response curves over the entire spectral range ($6\mu m < \lambda < 20\mu m$) of three different samples representing the short, mid and long peak wavelengths of the samples described in this work,

Fig. 3: Peak responsivity vs. bias for the different samples.

Fig. 4: Experimental and calculated peak wavelength as a function of the barrier Al concentration,

Fig. 5: Current-Voltage (l-V) curves of sample 1 at different temperatures. The dashed curve is the room temperature background photocurrent measured at 10K.

Fig. 6: Current-Voltage (l-V) curves of sample 4 at different temperatures, The dashed curve is the room temperature background photocurrent measured at 10K.

Fig. 7: Current-Voltage (I-V) curves of sample 5 at different temperatures. 'l'he dashed curve is the room temperature background photocurrent measured at 10K.

Fig. 8: Current-Voltage (l-V) curves of sample 7 at different temperatures. The dashed curve is the room temperature background photocurrent measured at 10K,

Fig. 9: Dark current vs. inverse temperature of sample 7 for different bias, the straight lines represent the thermally activated dark current while the leveling off at low temperature in due to tunneling.

Fig. 10: Normalized dark current (A/K) against reciprocal temperature showing the thermal activation of the dark current.

Fig, 11: Comparison between the cutoff wave] engtl obtained from the experimental spectra and that obtained from the thermal activation energy (plotted vs. barrier A concentration).

Fig. 12: Dynamic resistance vs. reciprocal temperature at -2Volt for the different samples.

Fig. 13: Net shot noise current as a function of the bias for the different samples at T= 55K.

Fig. 14: Optical gain, determined from the measured dark current noise for samples 1 and 7, representing the extremes of the sample spectra.

Fig. 15: Detectivity (D^*_λ) as a function of bias for sample 7 at 55K.

Fig. 16: Detectivity (D^*_λ) values of the different samples at 55K and -2V, (plotted against peak wavelength).

Table 1: Well width and Al concentration of the different samples

Sample	1	2	3	4	5	6	7
L_W(Å)	72	72	72	72	66	66	66
%Al	13.0	13.5	14.0	14.5	14.5	15.0	15.5

'I'able 11: Peak responsivity in A/W and V/W (at -2V and 55K) for the different samples as well as the peak and cutoff wavelengths and FWHM $\Delta\lambda$ (in μm and meV)

Sample	1	2	3	4	5	6	7
λ_p	17.5	16.8	16.5	15.9	1S.6	1s.3	15.0
λ_c	18.6	17.8	17.3	16.8	16.9	16.3	1s.9
$\Delta\lambda$	2.62μm 10.9meV	2.16μm 9.6meV	2.11μm 10.0meV	2.11μm 10.6meV	2.54μm 13.0meV	2.27μm 12.3meV	2.00μm 11.2meV
I?,>(A/W)	0.46	0.43	0.29	0.27	0.49	0.39	0.40
R,)(V/W)	3600	7900	16700	33000	32100	47500	87300

Table 11 I: Calculated parameters of the different QWI 1' structures

Sample	1	2	3	4	5	6	7
1st state (meV)	37.6	38.1	38.6	39.1	*43.1*	*43.7*	*44.2*
2nd state (meV)	111.4	114.9	118.1	*121.2*	124.1	*127.8*	*131.4*
Barrier height (meV)	112.0	116.1	120.1	124.1	124.2	128.2	132.2

'J'able IV: 111.11' temperature of the different samples

Sample	1	2	3	*4*	5	*6*	*7*
T_{BLIP} (K)	38.0	41.0	43.0	*4s.5*	*44.5*	*46.0*	*47.5*

'J'able V: Activation energy ($\Delta E = E_C - E_F$) as obtained from the normalized dark current vs. 1/T slope (upper row) and by the cutoff energy and Fermi level calculation (lower row)

Sample	1	2	3	4	5	6	7
ΔE (meV)	58.1	61.0	62.5	68.5	67.1	70.2	71.6
ΔE (meV)	60.2	6302	6 / 02	67.3	67.5	70.2	72.1

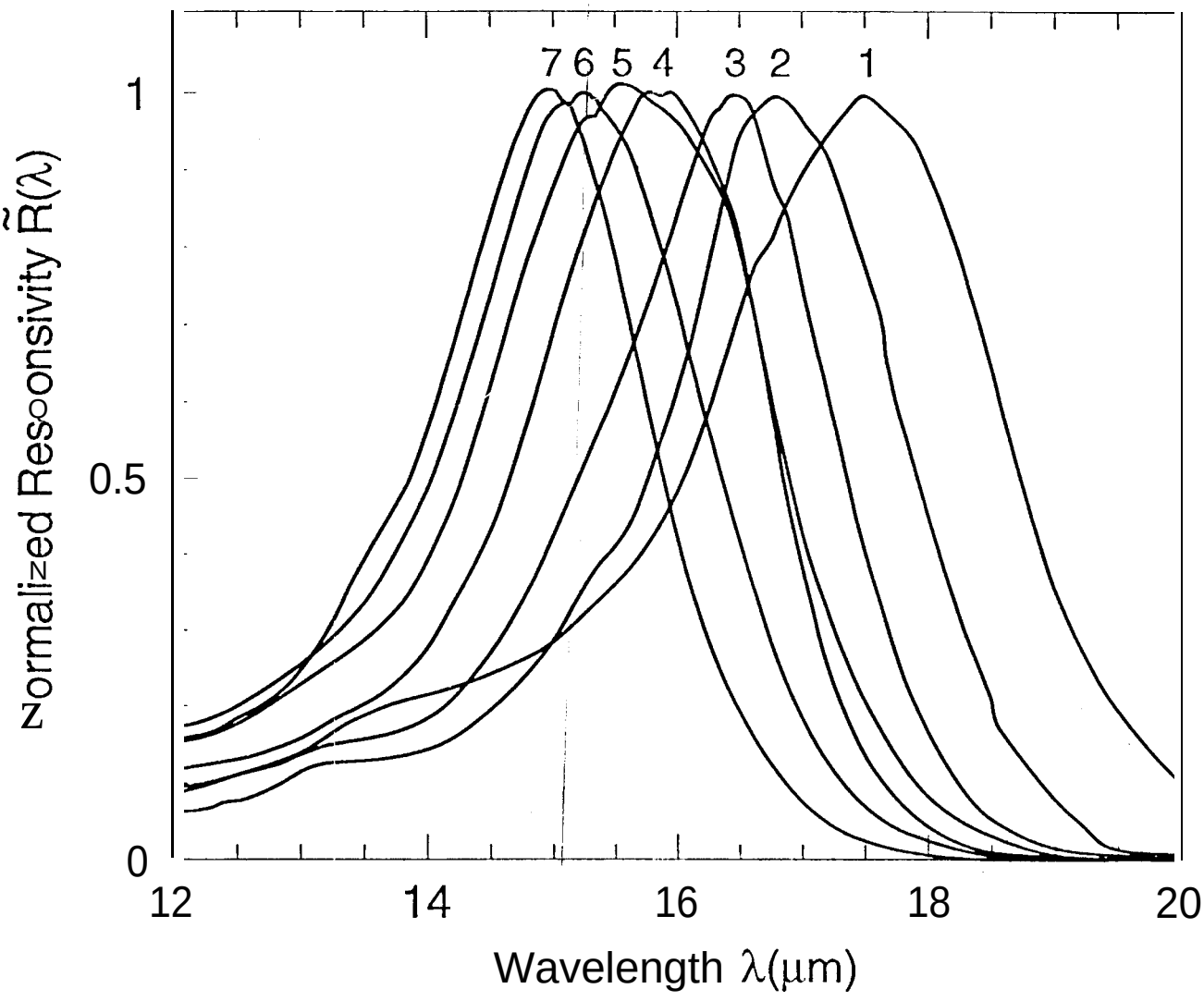

C&D 4M20687. 15

Fig. 1 Sarusi et al.

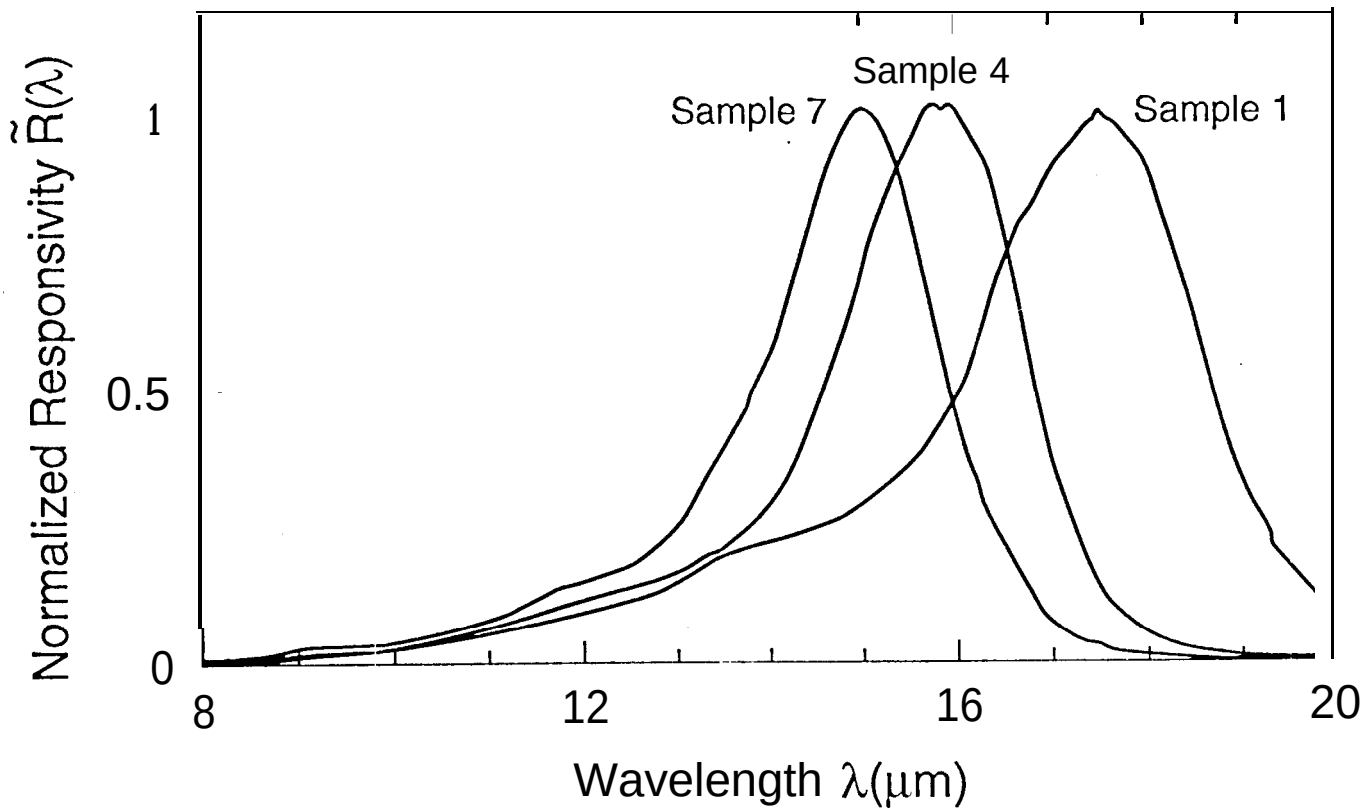

C&D 4M20687.16

Fig. 2 Sarusi et al.

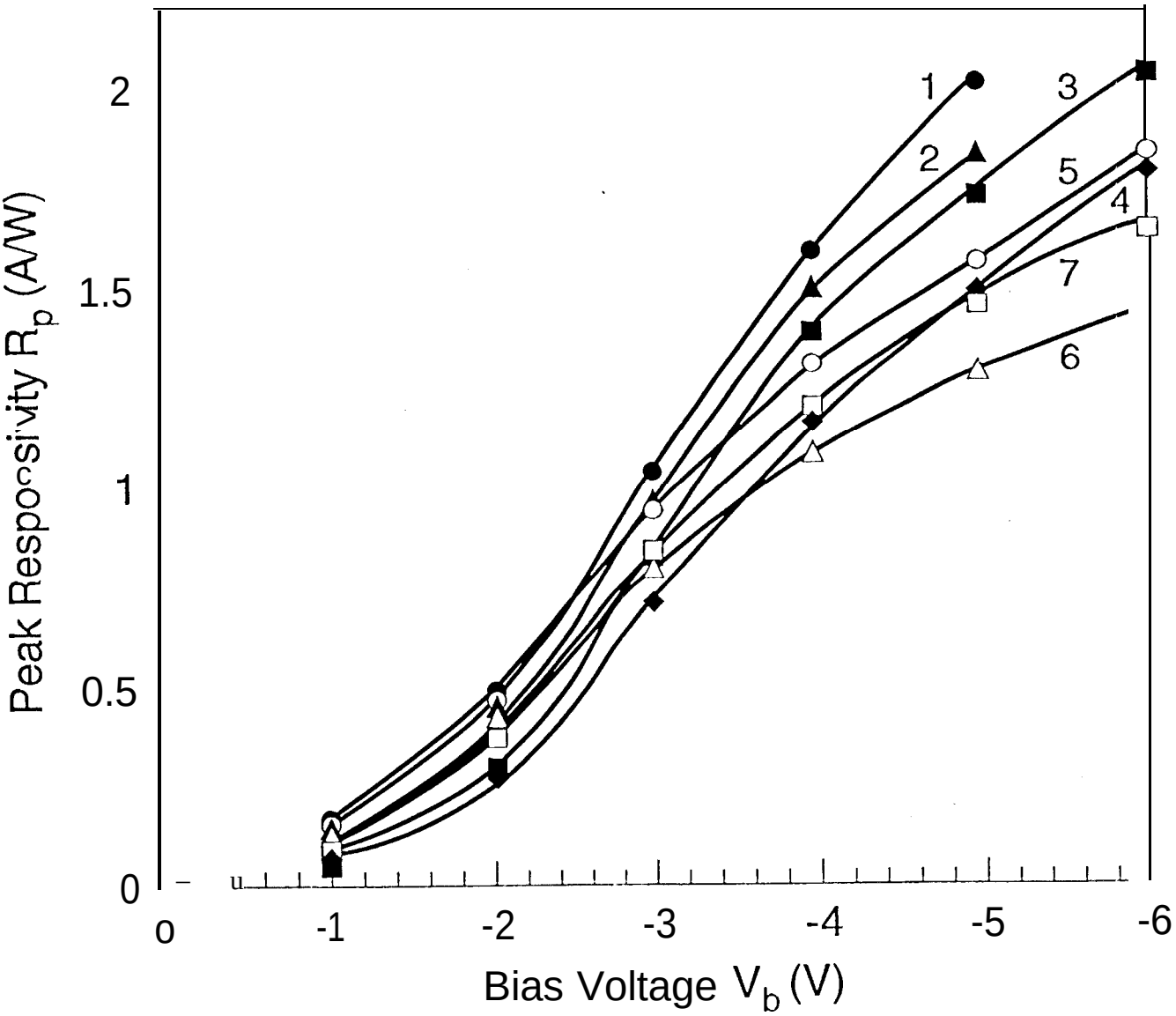

C&D 4M20687.9

Fig. 3 Sarusi et al.

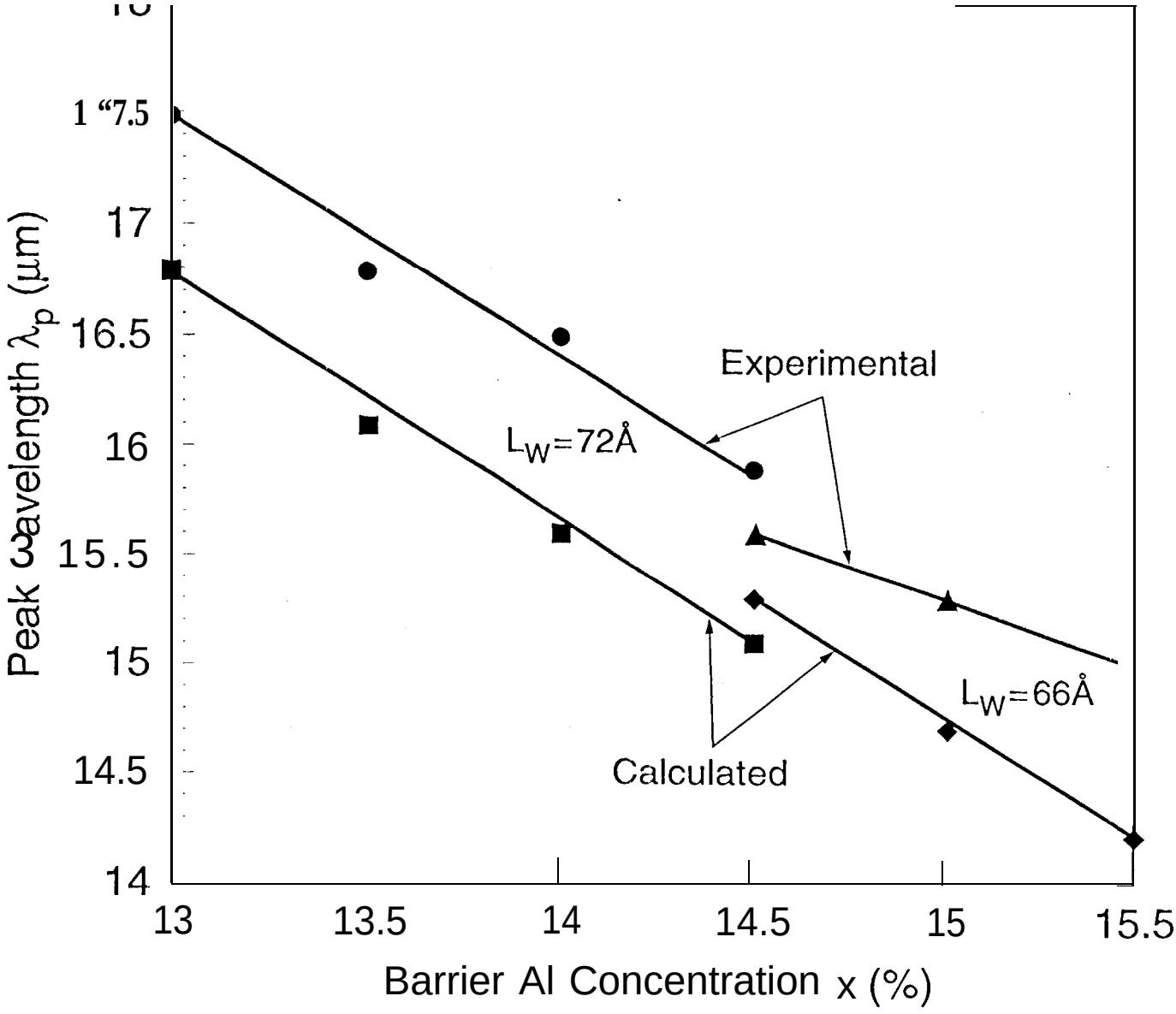

C&D 4M20687.10

Fig. 4 Sanuzi et al.

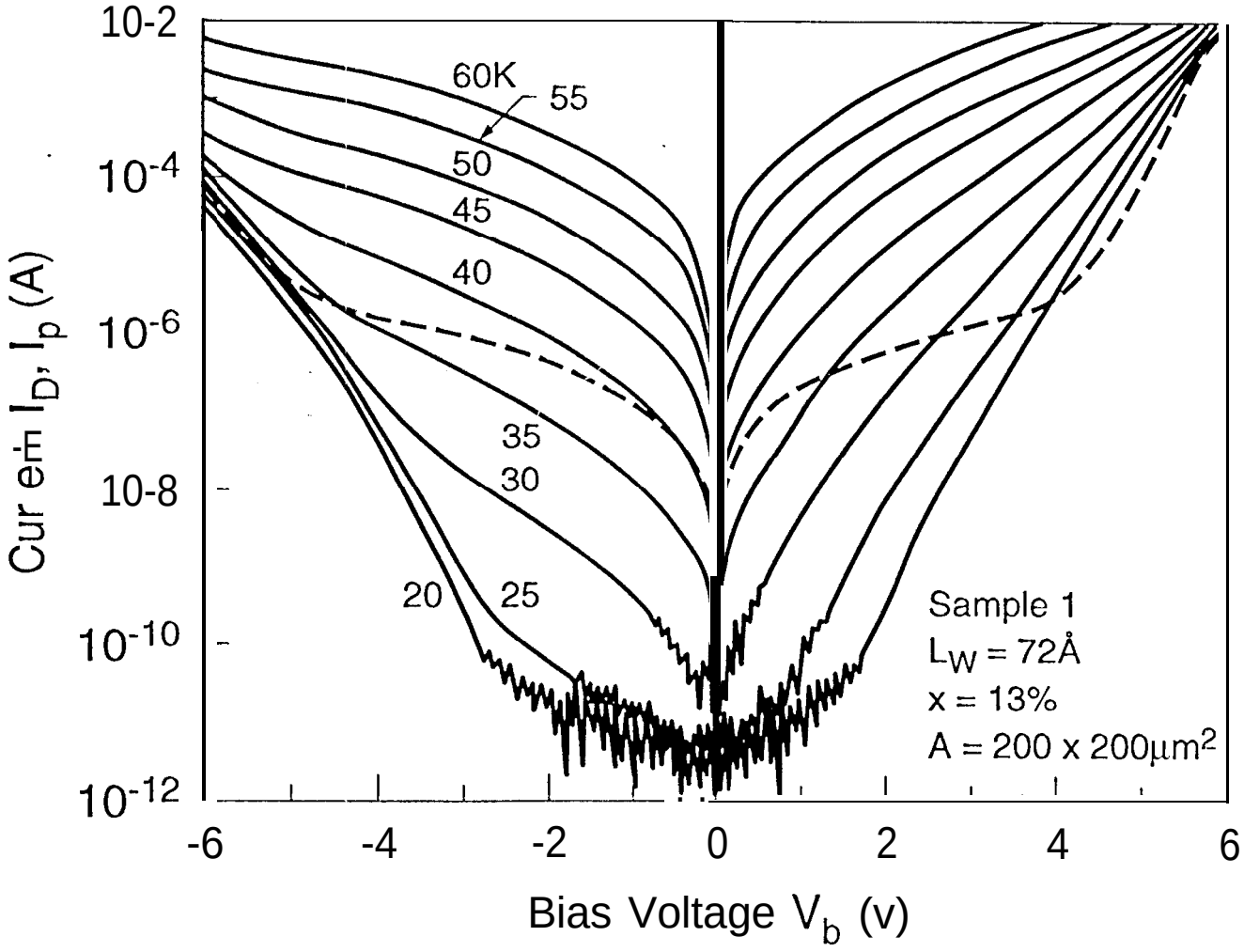

C& D 4M20687.11

Fig. 5 .54-44' et al.

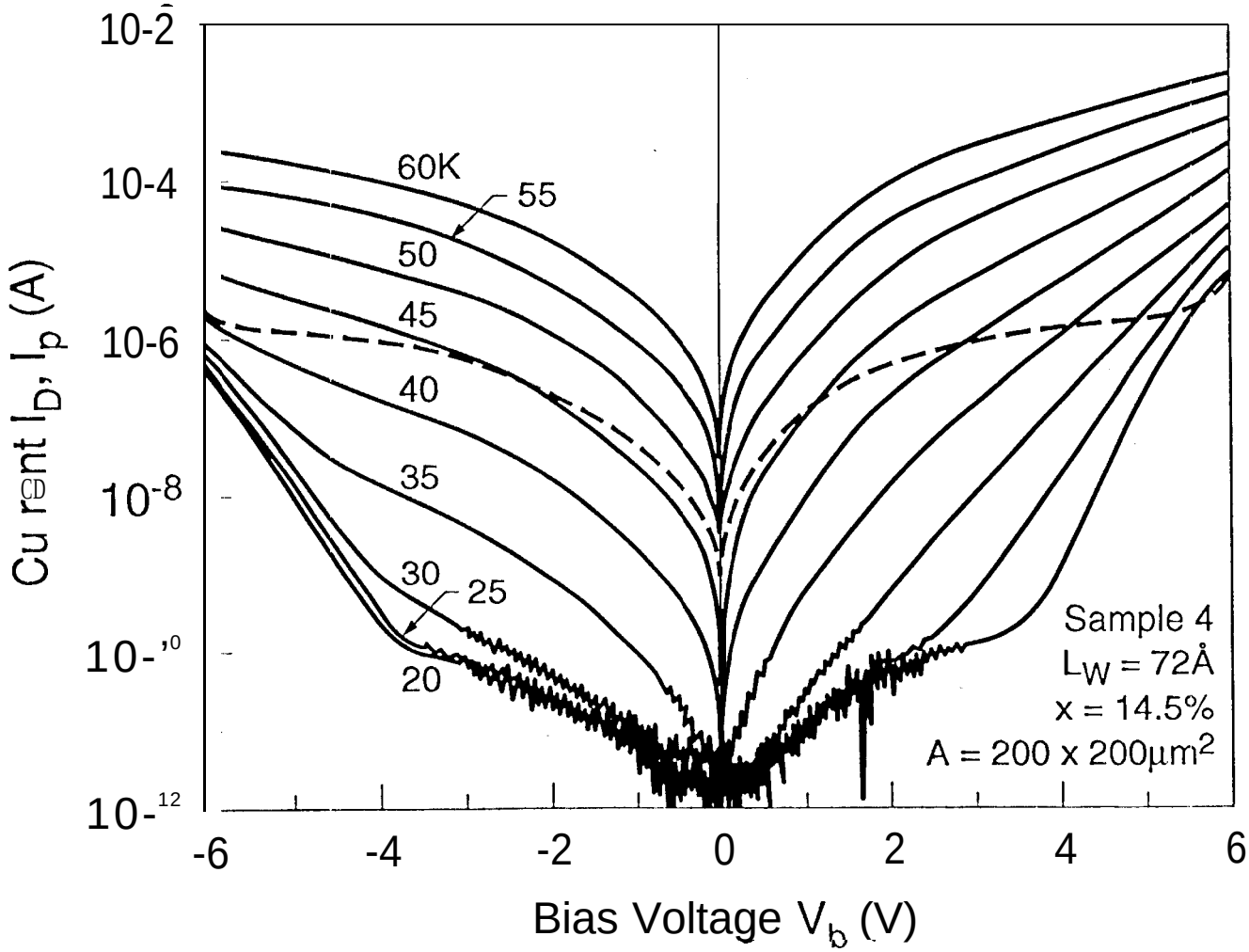

C&D 4M20687.12

Fig. 6 Sarusi et al.

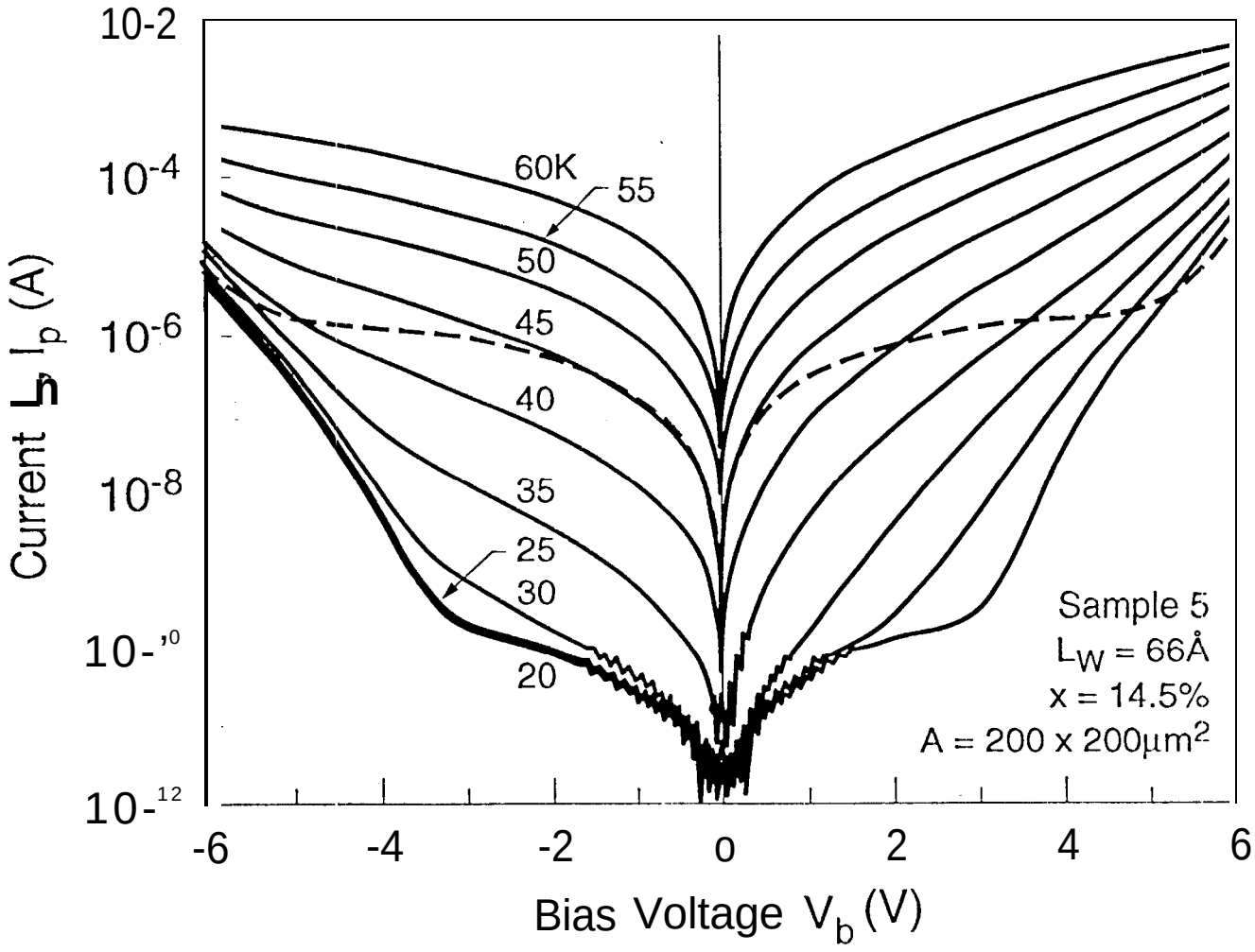

C&D 4M20687.13

Fig. 7 Sarusi et al.

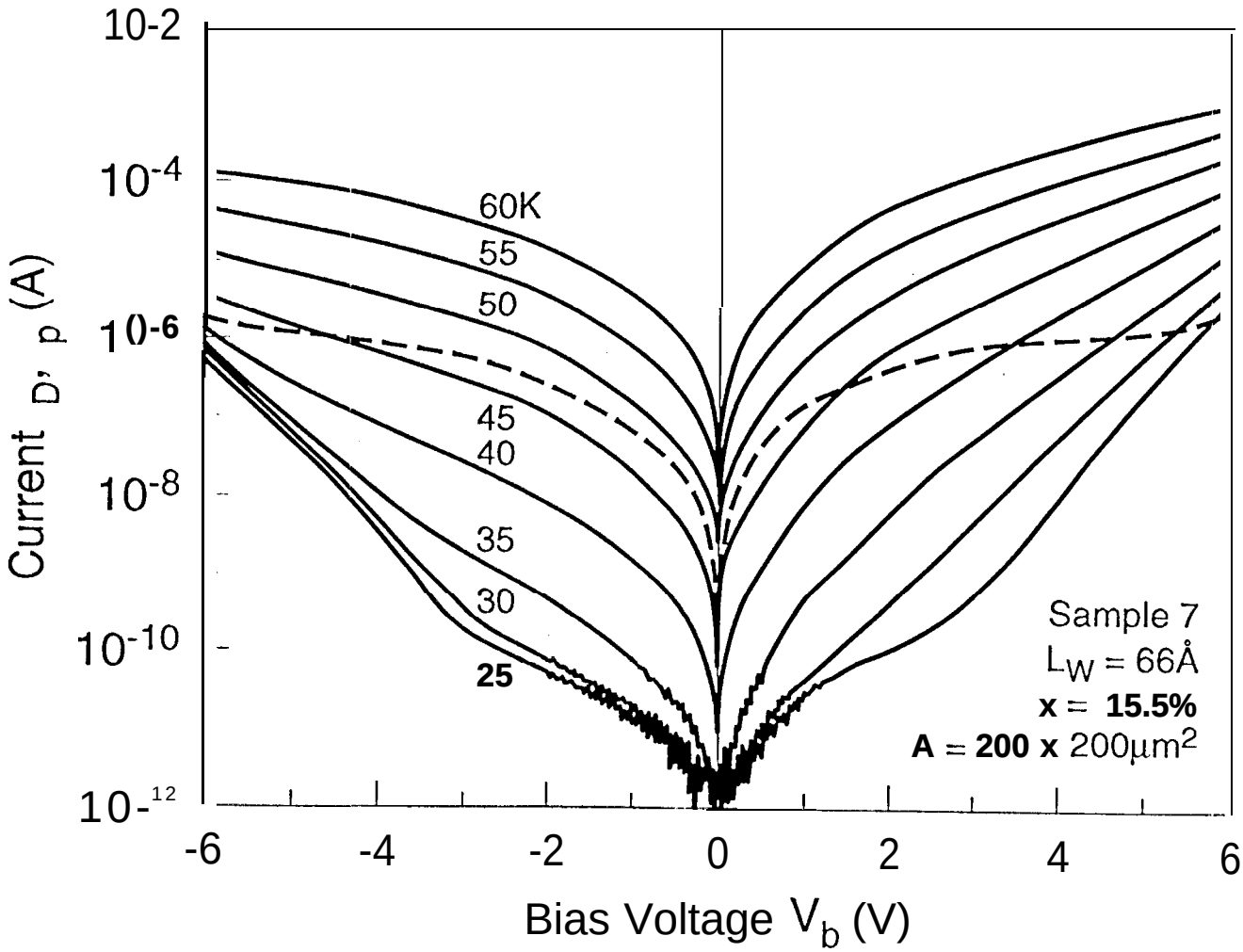

C&D 4M20687.14

Fig. 8 Sorusi et al.

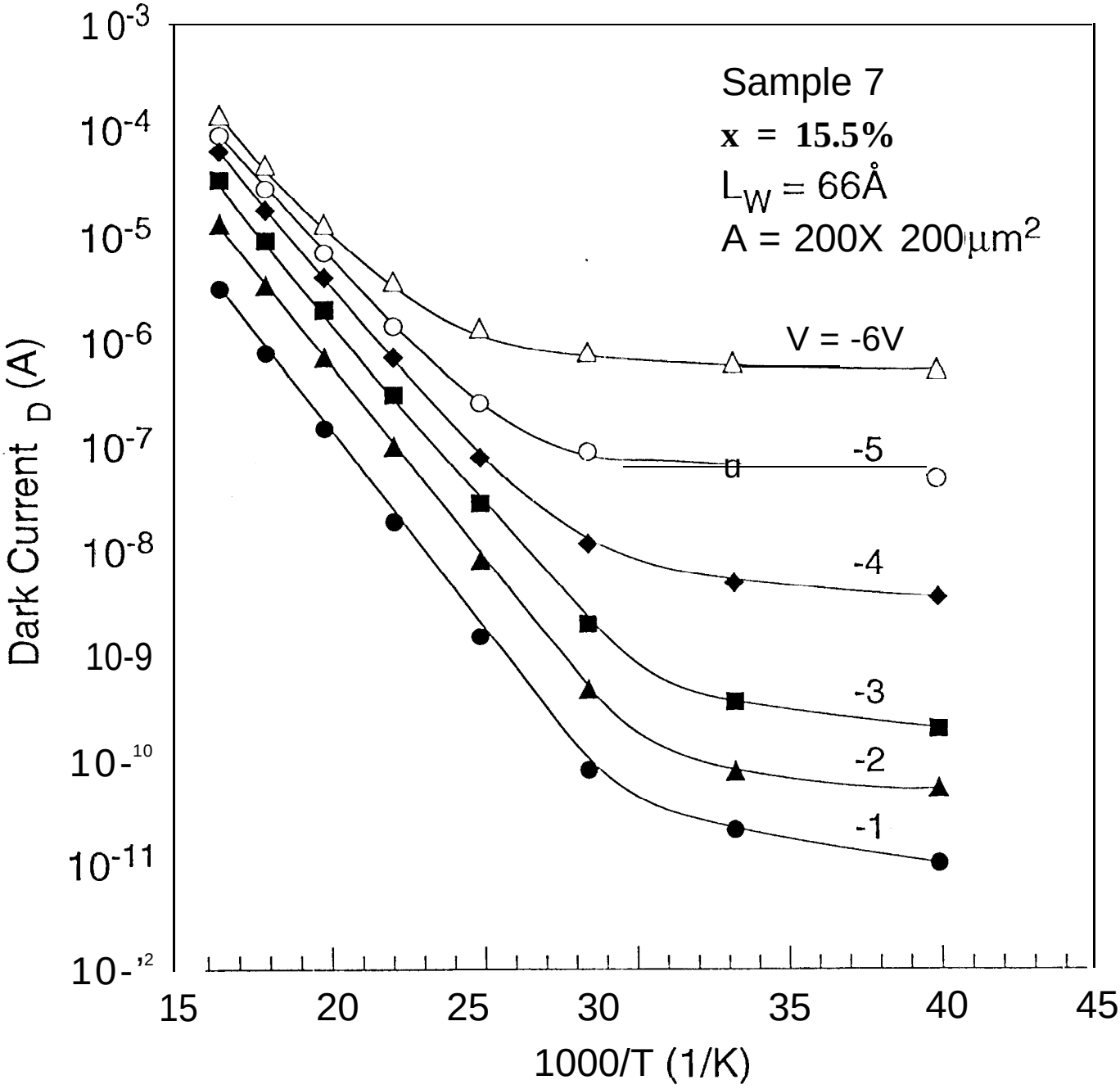

C&D 4M20687.8

Fig. 9 Sarusi et al.

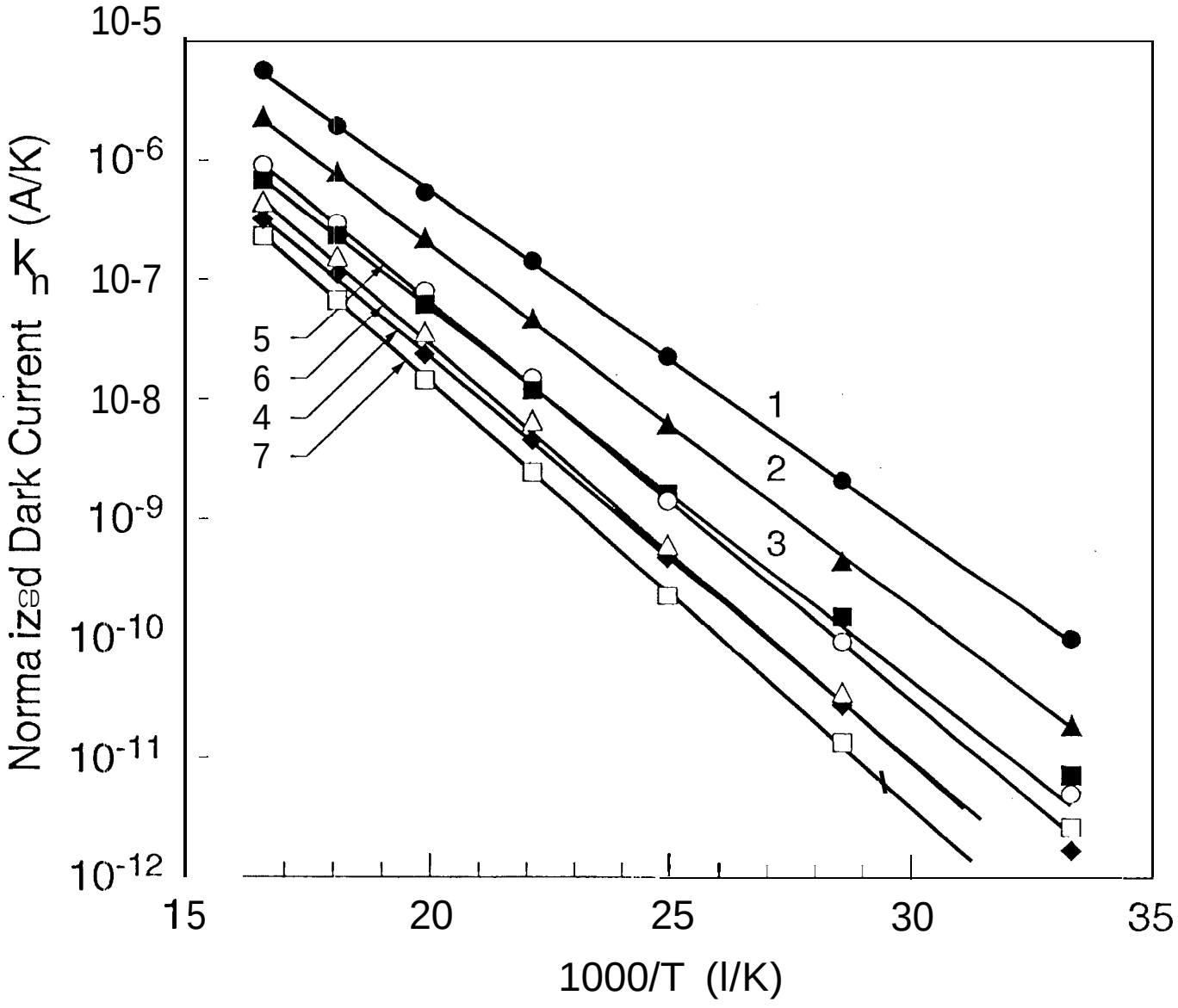

C&D 4M20687.7

Fig. 10 Sarusi et al.

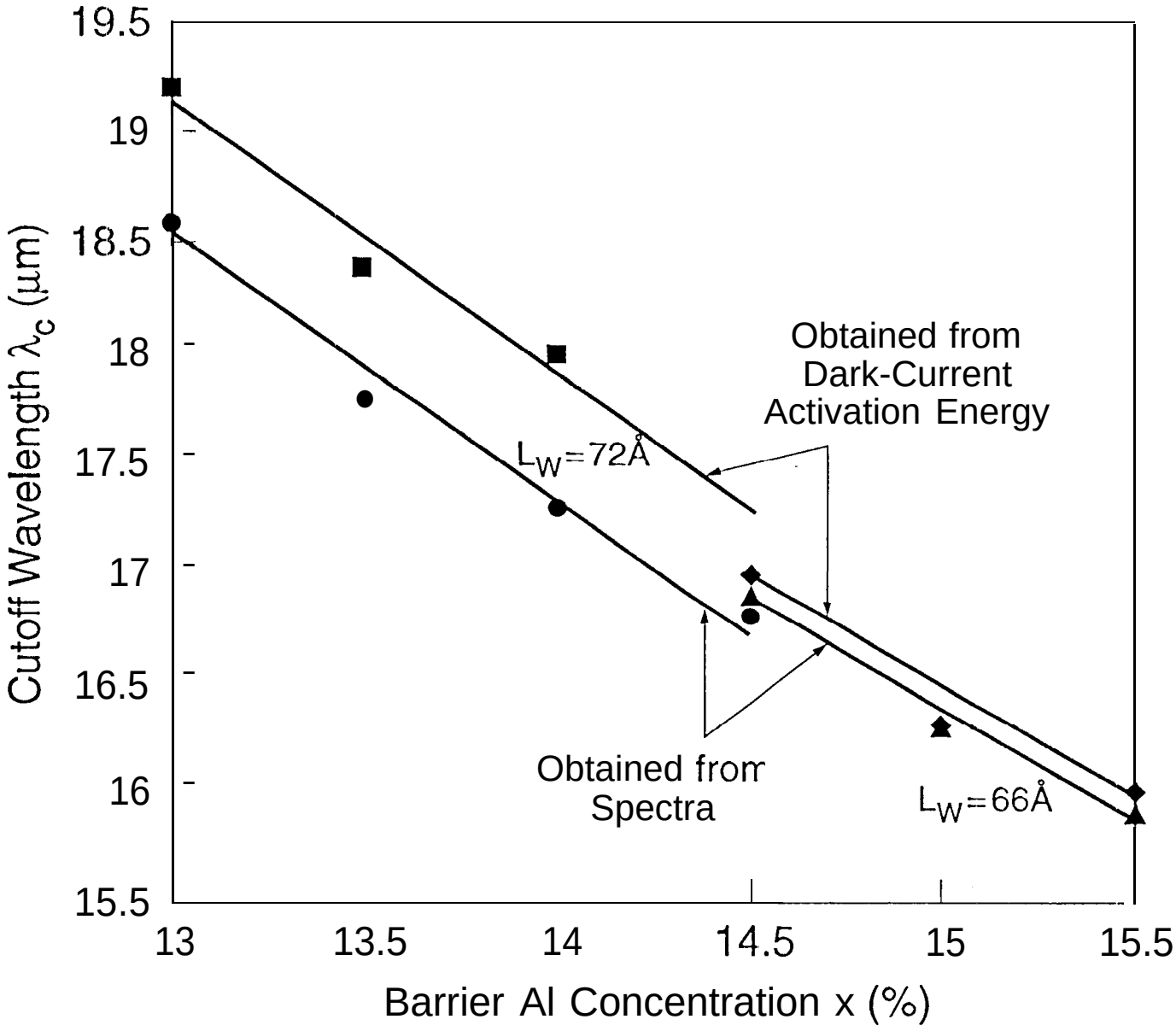

C&D 4M20687.6

Fig. 11 Sarusi et al.

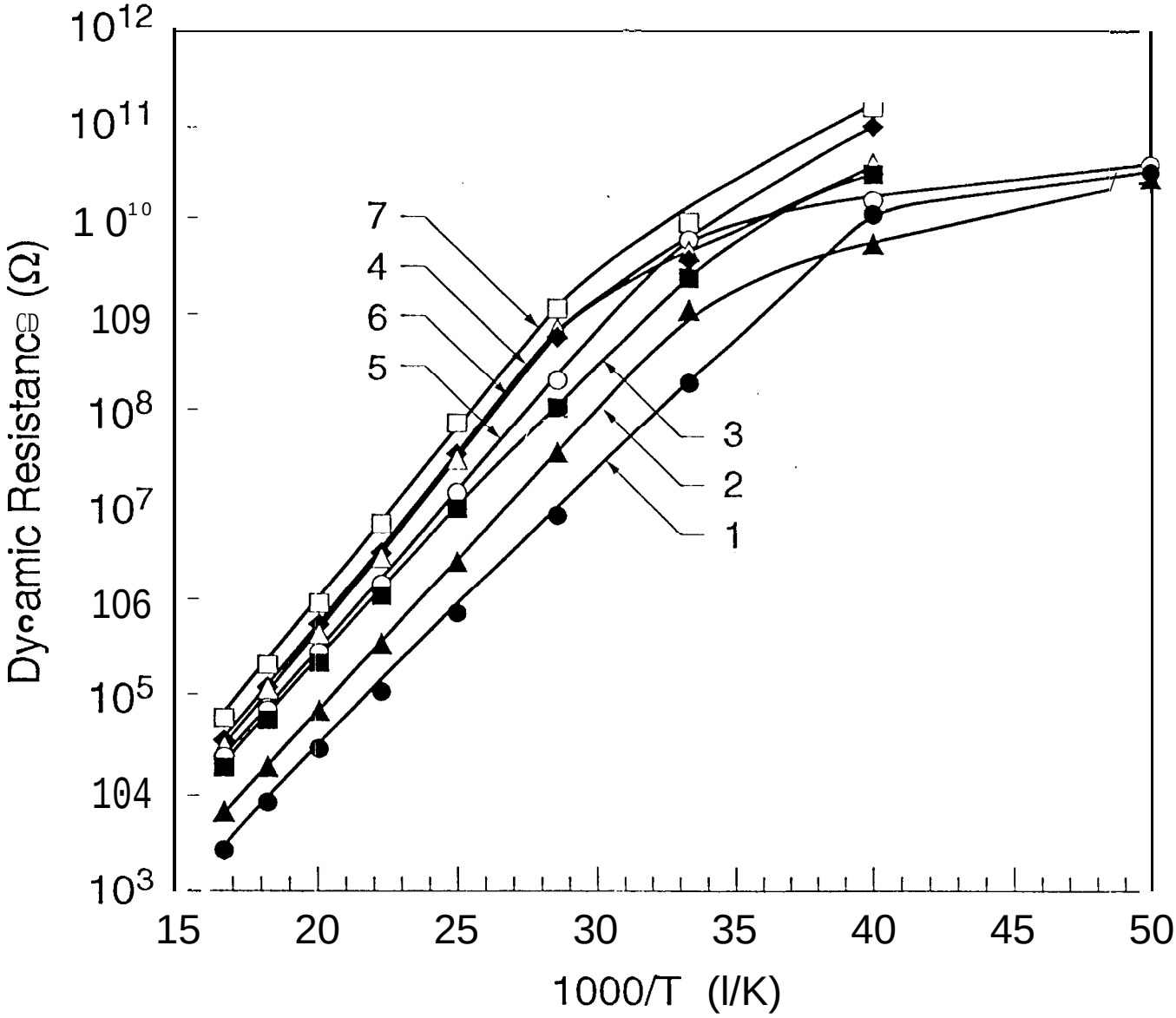

C&D 4M20687.5

Fig. 12 Sarusi et al.

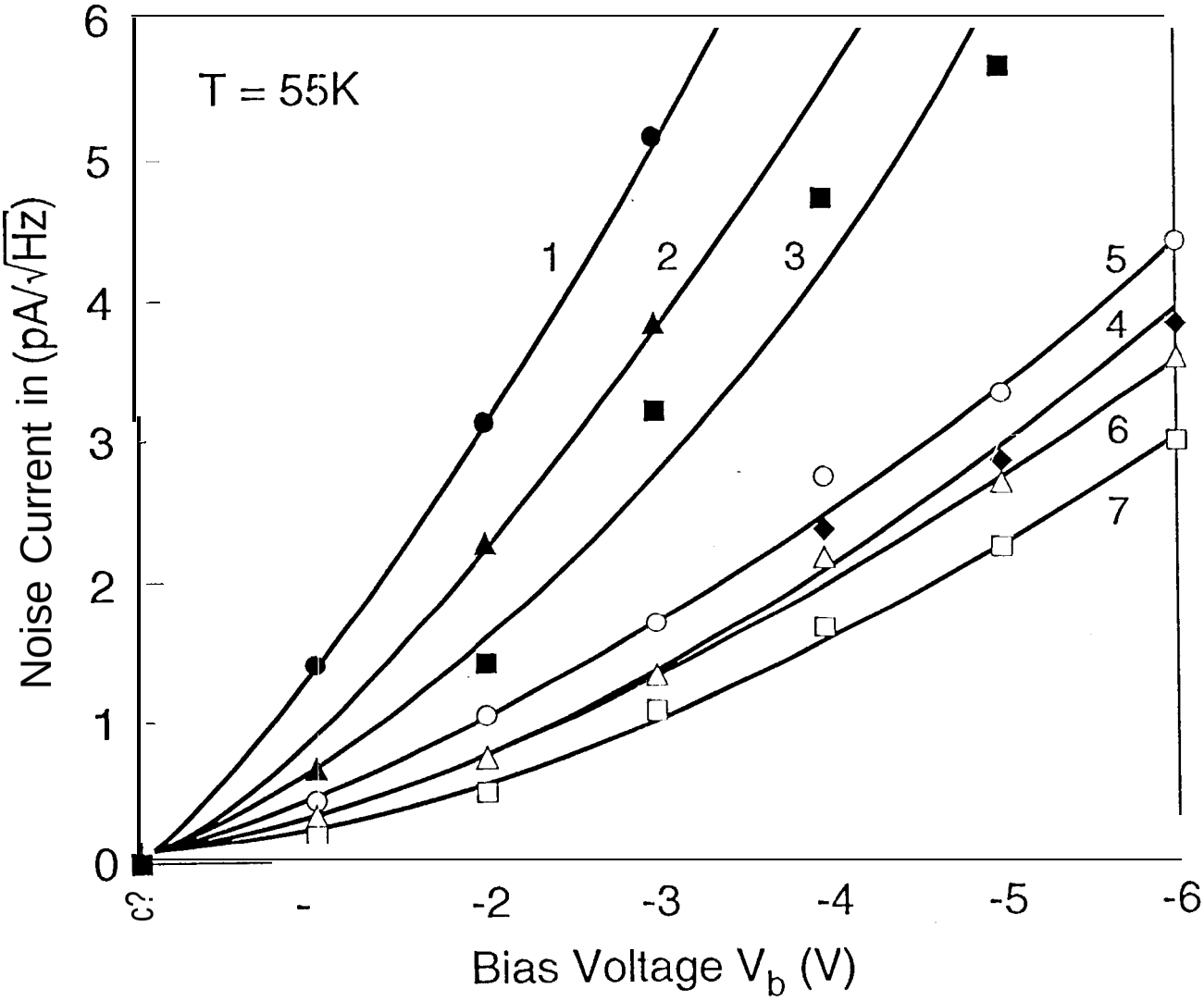

C&D 4M20687.4

Fig. 13 Sarusi et al

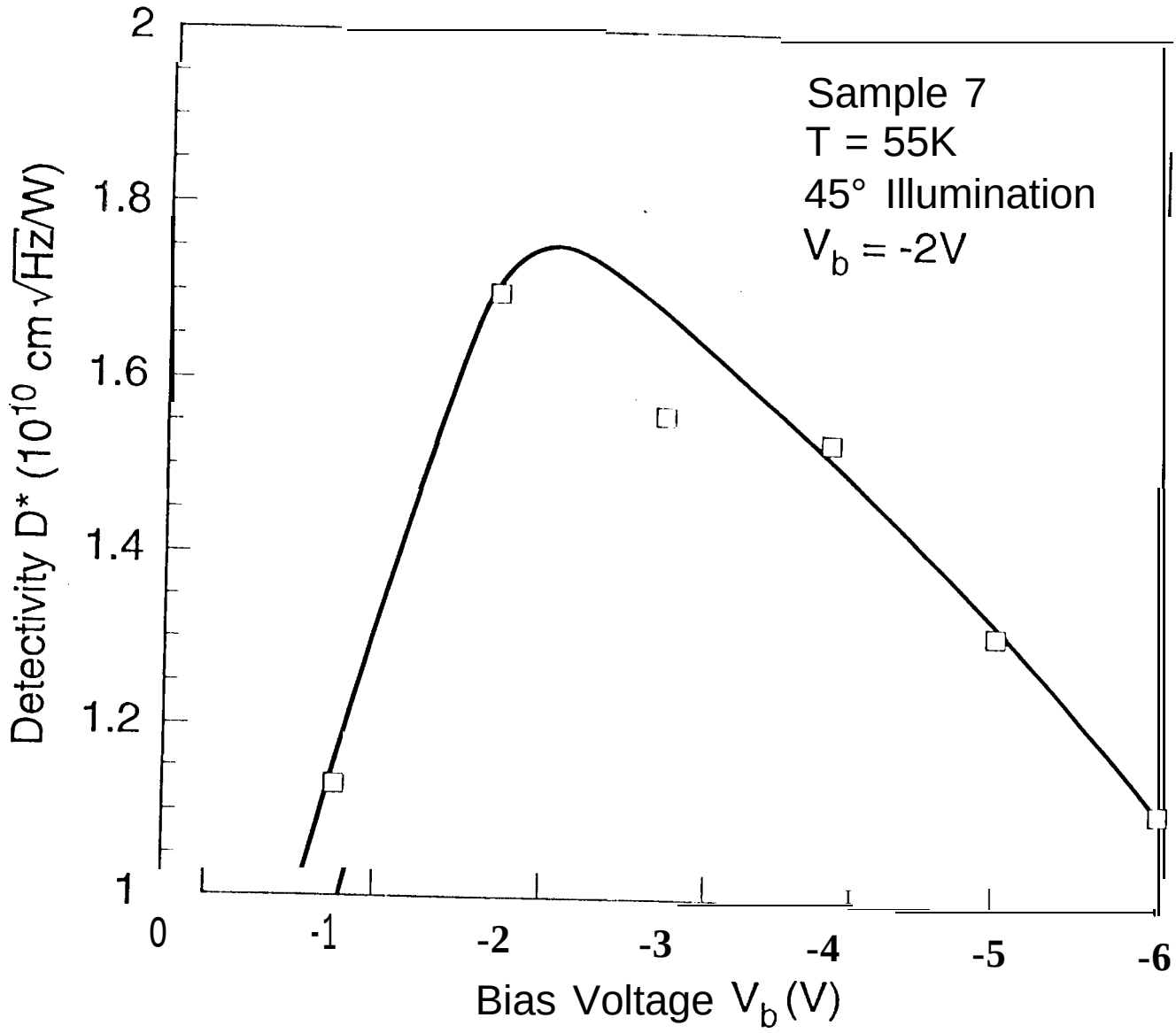

Fig. 15 Sarusi et al.

C&D 4M20687.2

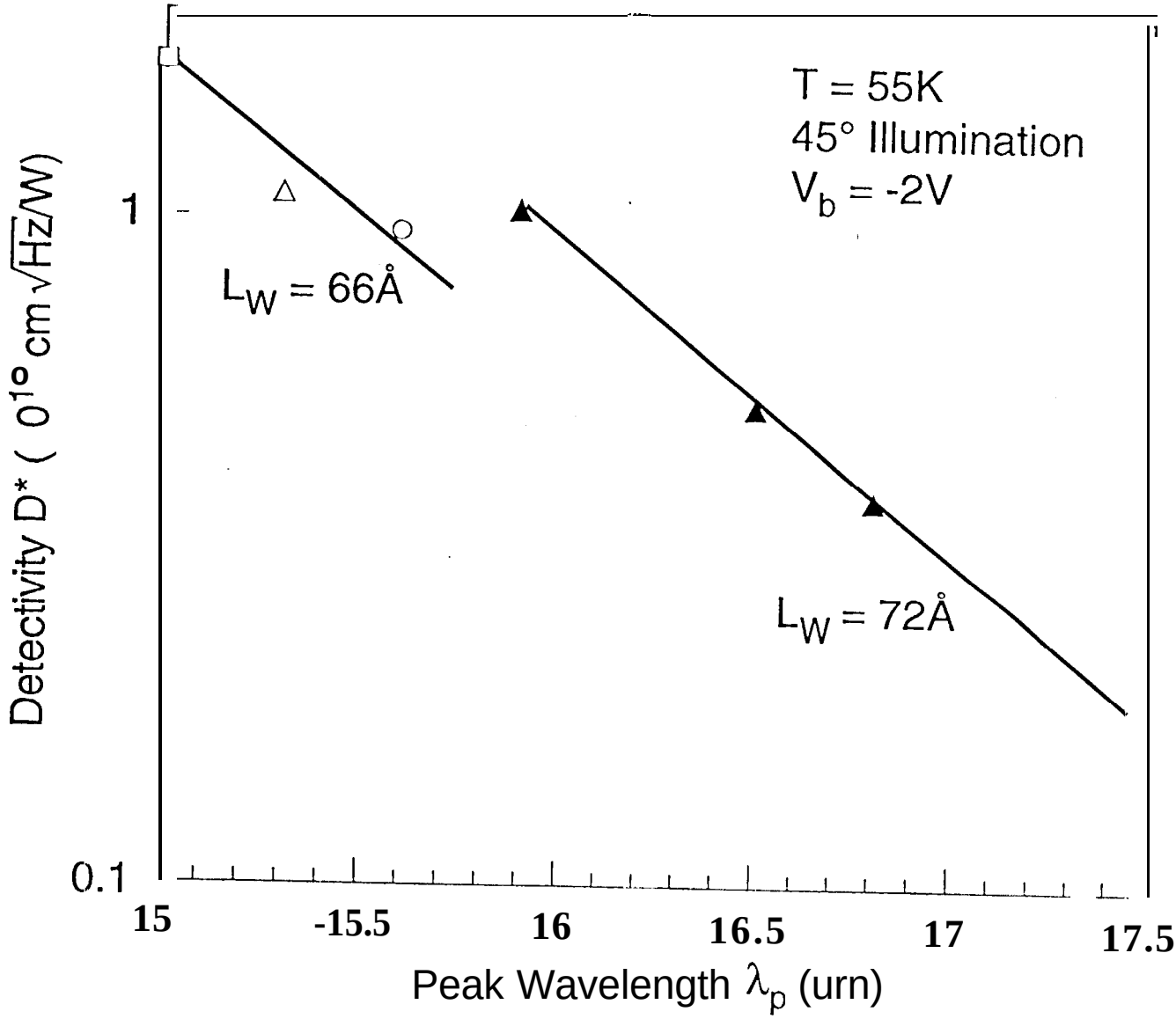

FIG. 16 Sarusi et al.

C&D 4M20687.1